A prediction-oriented hazard assessment procedure based on the empirical falsification principle, application to the Atenquique debris flow, 1955, México

Abani Patra[1,2], **Andrea Bevilacqua**[3,2,4], Marcus Bursik[3], E. Bruce Pitman[5], Dave Hyman[3,†], Ricardo Saucedo[6], José Luis Macìas[7]

(1) Department of Mechanical and Aerospace Engineering, UB, Buffalo, NY; (2) Computational Data Sciences and Engineering Program, UB, Buffalo, NY; (3) Department of Earth Sciences, UB, Buffalo, NY; (4) Istituto Nazionale di Geofisica e Vulcanologia, Sezione di Pisa, Pisa, Italy; (5) Department of Material Design and Innovation, UB, Buffalo, NY; (6) Instituto de Geología, Facultad de Ingeniería, UASLP, SLP; (7) Departamento de Vulcanología, Instituto de Geofísica, UNAM, DF; (†) now at CIMSS, UW, Madison, WI.

AGU100 ADVANCING EARTH AND SPACE SCIENCE
FALL MEETING
Washington, D.C. | 10–14 Dec 2018

Paper Number DI31B - 0001
Abstract ID: 422430

1. Prediction-oriented modeling

Hazard assessment of **geophysical mass flows**, such as landslides or pyroclastic flows, usually relies on the reconstruction of past flows that occurred in the region of interest using models of physics that have been successful in **hindcasting**. While **physical models** relate inputs and outputs of the dynamical system of the mass flow (Gilbert, 1991; Patra et al., 2018a) this relation is dependent on the choice of model and parameters which is usually difficult for future events.

Choices based on limited data using **classical inversion** is often misleading since it does not reflect all potential event characteristics and even in a probabilistic setting can be error-prone, due to incorrectly limited event space.
In this work, we use a **multi-model** ensemble and a **plausible region** approach to provide a more **prediction-oriented** probabilistic framework for hazard analysis.

In a **probabilistic framework**, for each model M_j we define a probability measure P_M over the measurable parts of its input space Ω^j_0. In the sequel we assume $P_M \sim \text{unif}(\Omega^j)$, where $\Omega^j \subseteq \Omega^j_0$ is called **specialized input space**.

We represent each model M_j with an operator: $f_{M_j} : \Omega^j_0 \longrightarrow \mathbb{R}^d$. The set of feasible inputs: $\Omega_G := \bigsqcup_j \Omega^j_0$, is a natural meta-modeling framework. Then, we characterize the codomain $D_G \subset \mathbb{R}^d$ of plausible outputs - it includes all the outputs consistent with the observed data, plus additional outputs which differ in arbitrary, but plausible ways (see Fig. 2).

The implementation of **multiple models** is a crucial aspect. Typically, a single model is not able to **entirely cover** Ω_0.

So ∀j, the specialized input space is defined by: $\Omega^j = f_{Mj}^{-1}[D_G \cap f_{Mj}(\Omega_0^j)]$. See Figure 1 and 2.
In a similar way, ∀i, the partial solutions to the inverse problem are: $\Omega_i^j = f_{Mj}^{-1}[D_i \cap f_{Mj}(\Omega^j)]$.

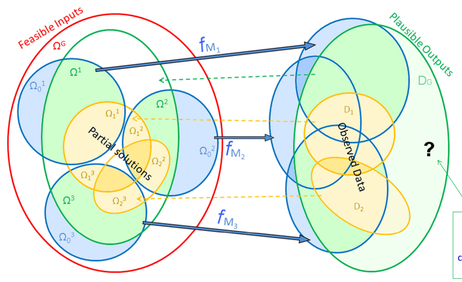

Fig 1. Venn Diagram:
- input spaces, output space, and model functions ,
- feasible inputs domain,
- plausible output codomain and specialized inputs,
- observed data and partial solutions.

The **question mark** emphasizes that the covering of other plausible outputs could be enabled, adding more models if necessary.

Fig 2. Diagram of the steps of our meta-modeling approach.

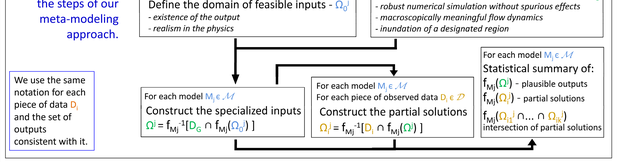

2. Geophysical models and input spaces

We adopt and compare the three depth averaged models **Mohr-Coulomb** (MC) (Savage&Hutter, 1989), **Pouliquen-Forterre** (PF) (Pouliquen, 1999; Pouliquen&Forterre, 2002) and **Voellmy-Salm** (VS) (Voellmy, 1955; Salm, 1990).

Input spaces are explored by **Latin Hypercube sampling** (McKay, 1979; Owen, 1992b; Stein, 1987). The models are incorporated in our large scale mass flow simulation framework **TITAN2D** (Patra et al., 2005; Patra et al., 2018b).

Models are parameterized by:

$$\Omega_0^{\text{MC}} = \left\{(\phi_{bed}, \phi_{int}, V) \in \mathbb{R}^3_+\right\} \qquad \Omega_0^{\text{PF}} = \left\{(\phi_1, \phi_2, L, V) \in \mathbb{R}^4_+\right\} \qquad \Omega_0^{\text{VS}} = \left\{[\arctan(\mu), \log_{10}(\xi), V] \in \mathbb{R}^3_+\right\}$$

– **Total Volume:** $V \in [3.5,\ 5] \times 10^6\ m^3$, i.e. $4.25 \pm 0.75 \times 10^6\ m^3$.

– **Input space constraints:**

MC - $\phi_{bed} \geq 5°, \quad \phi_{int} \in [\phi_{bed},\ 45°]$.

PF - $\phi_1 \geq 1°, \quad \phi_2 \in [\phi_1 + 6°,\ \phi_1 + 18°], \quad L \in [0.1,\ 0.5]\ m.$

VS - $\arctan(\mu) \geq 1°, \quad \log_{10}(\xi) \leq 4.$

Feasible inputs domain Ω_G

We enhance the sampling procedure by relying on orthogonal arrays (Owen, 1992a; Tang, 1993)

The 4th release of TITAN2D available from **vhub.org** offers multiple rheology options in the same code base.

∀j the construction of Ω^j relies on **extensive testing** of the models over the input space $\Omega_0^j \subseteq \Omega_G$. We adopt an itemized application of the **empirical falsification principle** of K.R. Popper (Popper, 1959).

We base our analysis on two qualitative properties that any **plausible output** must have:
(i) the flow must reach the town of Atenquique in a reasonable time (< 1200 s)
(ii) the flow does not unphysically run-up and over-spill the ravine walls for >0.1 m depth.

Figure 3 displays the plot of our specialized experimental design.

The existence of **multiple source areas** presents a unique challenge when attempting to model the considered flow (Saucedo, 2003; Saucedo et al., 2008). Based on the work in (Rupp, 2004) we initiate the flow from **five major** source locations, reported in Fig. 4. Piles are paraboloids with unit aspect ratio.

In particular, ∀ k, $w_k = V_k/V$ is:
$w_1 = w_3 = w_4 = 19.24\%$, $w_2 = 37.58\%$, $w_5 = 4.70\%$.

This is equivalent to choosing pile radii of 80 m, 100 m and 50 m respectively.

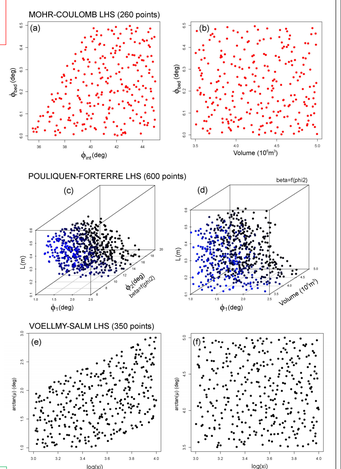

Fig 3. Overview of the specialized experimental design in (a-b) **MC**, (c-d) PF, (e-f) **VS** models. (a-c-e) are projected along the V coordinate, and (b-d-f) along ϕ_{int}, ϕ_2 and ξ coordinates, respectively.

An increase of w4, the source in Arroyo Seco,(Fig.4) is not excluded, but would require additional field work to be constrained.

In PF, the hue expresses the distance along the third dimension.

3. Geophysical case study and plausible outputs

The **Colima Volcanic Complex** is located in the western portion of the Trans-Mexican Volcanic Belt (small box in Fig.4). It consists of a N-S volcanic chain formed by Càntaro, **Nevado de Colima**, and Colima volcanoes (Allan, 1986; Robin et al., 1987; Luhr&Carmichael, 1990). Nevado de Colima (4320 m.a.s.l.) occupies the central part of the volcanic complex, being the most voluminous of the three volcanoes (Cortés et al., 2010).

The considered drainage starts at an elevation of **4000 m** on the eastern flank of Nevado, is occupied by **Atenquique river**, and ends at its junction with the Tuxpan River at **1040 m**. On 16 October, 1955, at 10:45 am, the inhabitants of Atenquique were surprised by the sudden arrival of an **8-9-m high** wave carrying mud, boulders and tree trunks. More than 23 people died, and the flood leveled everything but the tower of the church and the upper part of the market place (Ponce Segura, 1983; Saucedo et al., 2008).

Deposits cover a minimal area of 1.2 km², and a minimum volume of 3.2×10^6 m³ was estimated for the flow. The diluted flow that inundated the village probably had a velocity in the range of **4 to 6 m/s**, obtained by comparison with analogous flows (Pierson, 1985; Saucedo et al., 2008).

∀j we sample the model M_j input in a **Monte Carlo** simulation, and the output of each sample run is a function $f_j(\omega, \underline{x}, t)$, where ω is the input, t is the time and $\underline{x}$ is a spatial element of the computational grid. f_j is a **random function** with respect to the probability distribution P_{Mj} over Ω^j.
The results are summarized in Figure 5 by a family of spatial maps of **maximum flow depth** with respect to time, H.
We display the 5th and 95th percentiles with respect to P_{Mj}.

MC shows the lowest values, while **VS the highest**, especially in the distal part of the domain. In MC, the flow in the **tributaries** is not capable of reaching the village, while in the 95th percentile maps of PF and VS, it is. In VS, the flow in Arroyo Plàtanos joins the main ravine even in the 5th percentile map. Significant over-spill issues are absent.

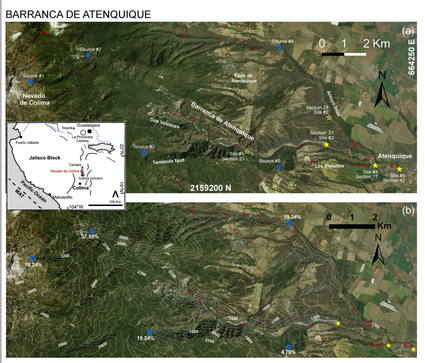

Fig 4. Barranca de Atenquique (MX) overview.
(a) sample sites of Saucedo et al., (2008) are marked with red dots, including 5 preferred locations (stars) and major ravines. Initial source piles are marked by blue dots. UTM zone 13N WGS84.

(b) Digital elevation map including isolines (NASA, 2014). Volume partition percentage among sources is reported. A regional map is in a small box.

Fig 5. Maximum flow height H as a function of time in (a-b) MC, (c-d) PF, (e-f) VS model. (a-c-e) are the 5th and (b-d-f) are the 95th percentile values with respect to P^j. Elevation contours are included at intervals of 100 m and 500 m (NASA, 2014).
Sites #3, #4, #5 are displayed.

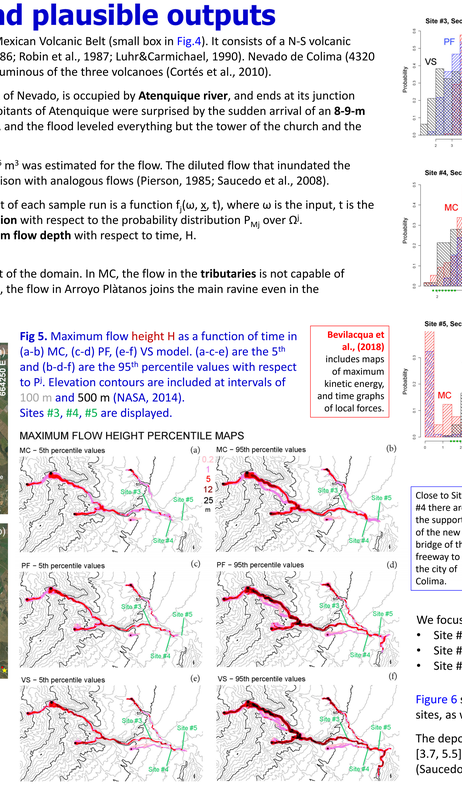

Bevilacqua et al., (2018) includes maps of maximum kinetic energy, and time graphs of local forces.

Close to Site #4 there are the supports of the new bridge of the freeway to the city of Colima.

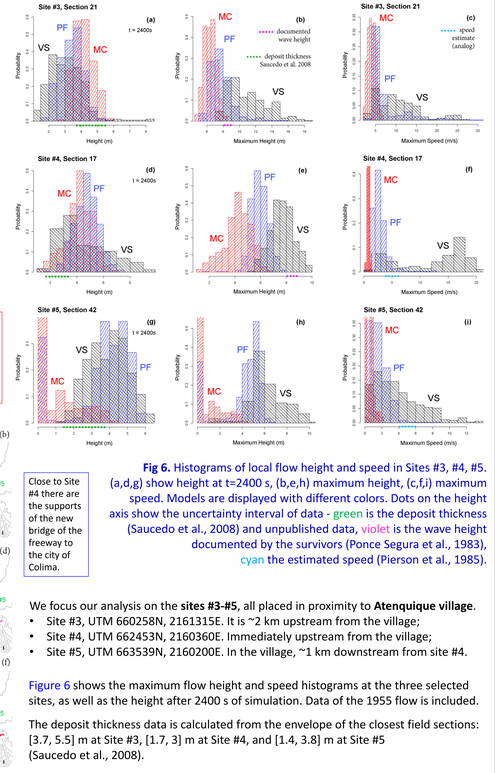

Fig 6. Histograms of local flow height and speed in Sites #3, #4, #5. (a,d,g) show height at t=2400 s, (b,e,h) maximum height, (c,f,i) maximum speed. Models are displayed with different colors. Dots on the height axis show the uncertainty interval of data - green is the deposit thickness (Saucedo et al., 2008) and unpublished data, violet is the wave height documented by the survivors (Ponce Segura et al., 1983), cyan the estimated speed (Pierson et al., 1985).

We focus our analysis on the **sites #3-#5**, all placed in proximity to **Atenquique village**.
- Site #3, UTM 660258N, 2161315E. It is ~2 km upstream from the village;
- Site #4, UTM 662453N, 2160360E. Immediately upstream from the village;
- Site #5, UTM 663539N, 2160200E. In the village, ~1 km downstream from site #4.

Figure 6 shows the maximum flow height and speed histograms at the three selected sites, as well as the height after 2400 s of simulation. Data of the 1955 flow is included.

The deposit thickness data is calculated from the envelope of the closest field sections: [3.7, 5.5] m at Site #3, [1.7, 3] m at Site #4, and [1.4, 3.8] m at Site #5 (Saucedo et al., 2008).

4. Partial solutions in the input space

Figure 7 shows the barplots of **data likelihood**. Model performance depends on the selected **type of data and site**.
- [**deposits height**] MC performs well at Site #3, while VS at Site #5.
- [**maximum flow height**] PF and VS can replicate the values at Site #3, and only VS can replicate the values at Site #4.
- [**maximum flow speed**] PF and VS perform moderately well at Site #4, while only VS at Site #5.

Figure 8 display two examples of **partial solutions** in the specialized experimental design.
For each example n=1,2 we select a **subfamily of empirical data** $(D_i)_{i \in I_n}$ and define, ∀ j:

$$\Theta^j_n := \bigcap_{i \in I_n} \Omega^j_i$$

Fig 7. Barplots of data likelihood in Sites #3, #4, #5. (a) compares flow height at t=2400 s with observed deposit thickness (Saucedo et al., 2008).

(b) compares maximum height and maximum speed with observed wave height (Ponce Segura et al., 1983) and analog flow speed (Pierson, 1985). Models are displayed with different colors.

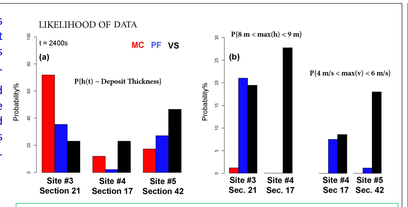

Fig.7a considers deposit thickness values, comparing them to the flow height at t=2400 s.

Fig 8. Example #1 of partial solution inputs in (a-b) MC, (c-d) PF, (e-f) VS.

The color expresses the considered data: yellow is deposit thickness in Site #5, blue is wave height in Site #4, red is flow speed in Site #5.

Example #2 of partial solution inputs in (a-b) MC, (c-d) PF, (e-f). Yellow is deposit thickness in Site #5, blue is wave height in Site #3, red is flow speed in Site #4.

(a-c-e) and (g-i-k) are projected along the V coordinate, and (b-d-f) and (h-j-l) along ϕ_{int}, ϕ_2 and ξ coordinates, respectively.

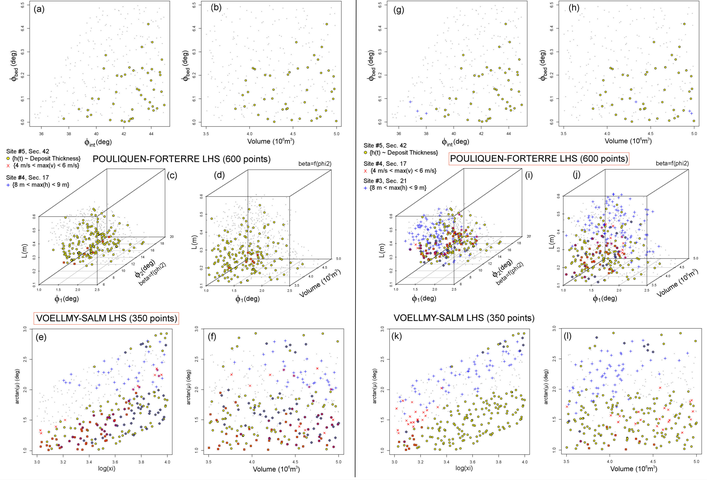

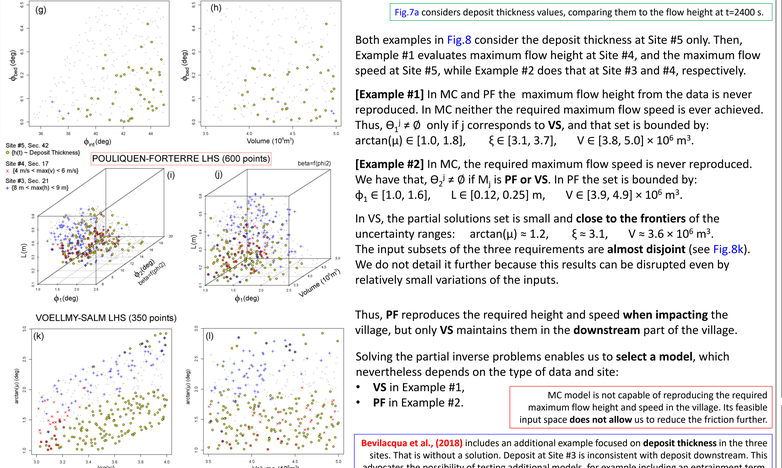

[Example #1] In MC and PF the maximum flow height from the data is never reproduced. In MC neither the required maximum flow speed is ever achieved. Thus, $\Theta_1^j \neq \emptyset$ only if j corresponds to **VS**, and that set is bounded by:
$\arctan(\mu) \in [1.0,\ 1.8], \quad \xi \in [3.1,\ 3.7], \quad V \in [3.8,\ 5.0] \times 10^6\ m^3$.

[Example #2] In MC, the required maximum flow speed is never reproduced. We have that, $\Theta_2^j \neq \emptyset$ if M_j is **PF or VS**. In PF the set is bounded by:
$\phi_1 \in [1.0,\ 1.6], \quad L \in [0.12,\ 0.25]\ m, \quad V \in [3.9,\ 4.9] \times 10^6\ m^3$.

In VS, the partial solutions set is small and **close to the frontiers** of the uncertainty ranges: $\arctan(\mu) \approx 1.2$, $\xi \approx 3.1$, $V \approx 3.6 \times 10^6\ m^3$.
The input subsets of the three requirements are **almost disjoint** (see Fig.8k). We do not detail it further because this results can be disrupted even by relatively small variations of the inputs.

Thus, **PF** reproduces the required height and speed **when impacting** the village, but only **VS** maintains them in the **downstream** part of the village.

Solving the partial inverse problems enables us to **select a model**, which nevertheless depends on the type of data and site:
- **VS** in Example #1,
- **PF** in Example #2.

MC model is not capable of reproducing the required maximum flow height and speed in the village. Its feasible input space **does not allow** us to reduce the friction further.

Bevilacqua et al., (2018) includes an additional example focused on **deposit thickness** in the three sites. That is without a solution. Deposit at Site #3 is inconsistent with deposit downstream. This advocates the possibility of testing additional models, for example including an entrainment term.

5. Examples of conditional results

The connection of inverse problems and model uncertainty is a challenge in the future development of multi-model solvers

In Figure 9 we report the spatial maps of mean of maximum in **flow height**, H, and **kinetic energy** κ. We report the histograms of maximum **dynamic pressure** Q.

$$\kappa := \frac{1}{2}\frac{(h\bar{u})^2 + (h\bar{v})^2}{h} \qquad Q := \max_{t \in T} \frac{\kappa}{h}$$

The dynamic pressure Q and the kinetic energy κ are scaled for a mass with unit density.

In Example #1, Q∈ [0, 150] m^2/s^2 at Site #4, Q∈ [7.5, 17.5] m^2/s^2 at #5.
In Example #2, Q∈ [8, 13] m^2/s^2 at Site #4, Q∈ [4, 7] m^2/s^2 at #5.
Typical values of density of **mudflows** are above 2000 kg/m³.

The [4, 6] m/s constraint on maximum flow speed has an **immediate** effect on Q. Imposing it at Site #5, as in the Example #1, or Site #4, as in the Example #2, radically changes the results.

More information on the **speed in the village** could allow us to further discriminate the models.

In the spatial maps of Fig.9, **PF** shows slightly lower maximum flow height, and significantly lower energy than **VS**, especially in the distal part of the domain.

The flow in the **tributaries** can reach the village, except for the smallest flows of Arroyo Plàtanos in PF, which however are only tens of meters from the main branch.

Local maxima of flow height are located in the ravine, while the kinetic energy shows a more regular decrease.

These conditional results focus on the replication of specific properties of the 1955 flow. They are enveloped in the wide range of plausible outputs displayed in Fig.5.

Fig 9. (a-b-c) Flow properties of VS model, in Example #1.
(d-e-f) Flow properties of PF model, in Example #2.

(a-d) Histograms of maximum dynamic pressure in Sites #4 and #5. Mean values of the maps of (b-e) maximum kinetic energy and (c-f) flow height as a function of time. Colors are related to their values. Elevation contours are at intervals of 100 m and 500 m (NASA, 2014).

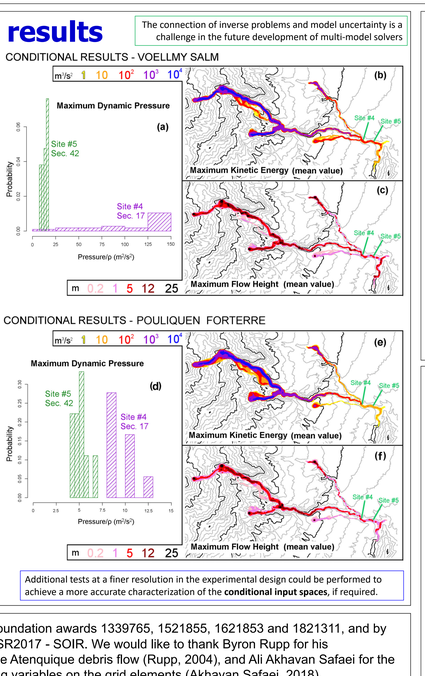

Additional tests at a finer resolution in the experimental design could be performed to achieve a more accurate characterization of the **conditional input spaces**, if required.

6. Conclusions

Similar strategies have been applied in hurricane hazard analysis (Krishnamurti et al., 2016; Ghosh et al., 2018).

We introduced a new prediction-oriented method for hazard assessment of debris flows.

In summary:
- We defined a **specialized experimental design** after assuming: the realism of the underlying physics, the numerical simulation robustness, and the meaningfulness of flow dynamics and inundation output. This contains valuable information for hazard assessment and this is a first step towards the development of an objective and **partially automated experimental design**.
- We calculated the **likelihood** that different model realizations reasonably represented the 1955 Atenquique flow, given **multiple pieces of field data**. The exercise provided useful information in either model selection or data inversion.
- We constructed **partial solutions to the inverse problem**, conditioning the specialized experimental design to be consistent with subsets of the observed data. We found **model selection** to be inherently linked to the inversion problem.
- Our results are consistent with **evolution of flow rheology** downstream in the vicinity of the village, from MC above the village, to either PF or VS within and downstream from the village. The meaning may reflect an evolution from inertial to macroviscous debris flow behavior near Atenquique.

Acknowledgements: This work is supported by National Science Foundation awards 1339765, 1521855, 1621853 and 1821311, and by Italian Ministry of Education, University, and Research, project FISR2017 - SOIR. We would like to thank Byron Rupp for his fundamental work on the localization and volume constraints of the Atenquique debris flow (Rupp, 2004), and Ali Akhavan Safaei for the C++ and Python scripts to collect the local outputs and contributing variables on the grid elements (Akhavan Safaei, 2018).

References: Akhavan Safaei, A. (2018). Master's Thesis, University at Buffalo.
Allan, J. (1986), Geological Society of America Bulletin, 97, 473–485.
Cortés, A. et al. (2010), Geological Society of America, Special paper, 464.
Ghosh, T. and Krishnamurti, T. N. (2018), Weather and Forecasting, 33, 873–885.
Gilbert, S. (1991), Journal of Research in Science Teaching, 28, 73–79.
Krishnamurti, T.N. et al. (2016), Reviews of Geophysics, 54, 336–377.
Luhr, J. and Carmichael, J. (1990), Geology of the Volán de Colima, Universidad Nacional de México.
McKay, M.D., Beckman, R. J., and Conover, W. J. (1979), Technometrics, 21, 239–245.
NASA (JPL) (2014), Shuttle Radar Topography Mission (SRTM), Tech. rep.
Owen, A.B.(1992a), Statistica Sinica, 2, 439–452.
Owen, A.B.(1992b), Journal of the Royal Statistical Society., 54, 541–551.
Patra, A. et al. (2005), Journal of Volcanology and Geothermal Research, 139, 1–21.
Patra, A., Bevilacqua, A. et al. (2018a), Lecture Notes in Computer Science, 10861, 724–736.
Patra, A., Bevilacqua, A. et al. (2018b), arXiv.org, 1805.12104, 1–39.
Pierson, T. (1985), Geological Society of America Bulletin, 96, 1056–1069.
Ponce-Segura, J. (1983), Historia de Atenquique, Talleres litográficos Vera.
Popper, K. R. (1959), The Logic of Scientific Discovery, Routledge.
Pouliquen, O. (1999), Physics of Fluids, 11, 542–548.
Pouliquen, O. and Forterre, Y. (2002), Journal of Fluid Mechanics, 453, 133–151.
Robin, C. et al. (1987), Journal of Volcanology and Geothermal Research, 31, 99 – 113.
Rupp, R. (2004). Master's thesis, University at Buffalo.
Salm, B. (1993), Annals of Glaciology, 18, 221–226.
Saucedo, R. (2003), Regional Geomorphology Conference, Mexico City, Mexico.
Saucedo, R., Macías, J.L., et al. (2008), Journal of Volcanology and Geothermal Research, 173, 69–83.
Savage, S.B. and Hutter, K. (1989), Journal of Fluid Mechanics, 199, 177-215.
Stein, M. (1987), Technometrics, 29, 143–151.
Tang, B. (1993), Journal of the American Statistical Association, 88, 1392–1397.
Voellmy, A.(1955), Schweiz Bauzeitung, 73, 159–165, 212–217, 246–249, 280–285.

Bevilacqua et al. (2018), Probabilistic forecasting of plausible debris flows from Nevado de Colima (Mexico) using data from the Atenquique debris flow, 1955. https://doi.org/10.5194/nhess-2018-294.